

# Cuprous Oxide Nanoshells with Geometrically Tunable Optical Properties

Li Zhang and Hui Wang\*

Department of Chemistry and Biochemistry, University of South Carolina, Columbia, South Carolina 29208, United States

Hollow nanostructures, also known as nanoshells, have attracted increasing attention because of their unique physical and chemical properties that allow them to be widely used as nanoscale chemical reactors,<sup>1,2</sup> high-performance catalysts,<sup>3,4</sup> drug-delivery carriers,<sup>5,6</sup> lithium-ion battery materials,<sup>7,8</sup> and subwavelength optical components for biomedical applications.<sup>9,10</sup> For photonic applications, materials with tunable optical responses over broad spectral ranges are highly desirable in many cases, and how to achieve such optical tunability has long been a key challenging issue. The nanoshell structures provide a unique geometry that can exhibit much more sensitive optical tunability than their counterparts with solid interior structures and are thus more desirable for a variety of optical applications.<sup>11,12</sup> This is essentially because in addition to the overall particle size and shape, nanoshells possess a unique geometrical parameter, the aspect ratio between the inner and outer dimensions, that one can adjust to further fine-tune the optical properties of the particles. One striking example is the noble metal nanoshells whose optical properties can be fine-tuned over a broad spectral range all the way across the visible and near-infrared regions by judiciously tailoring the inner and outer radii of the metallic shell.<sup>11–14</sup> The optical tunability of the metallic nanoshells can be theoretically interpreted in the context of the plasmon hybridization model in which the geometrically tunable nanoshell plasmon resonances are described as a result of the interactions between the plasmons supported by the inner and outer surfaces of the metallic shell.<sup>15,16</sup> In this paper, we investigate the optical tunability of Cu<sub>2</sub>O nanoshells as a nonplasmonic model system to demonstrate that geometrically tunable optical properties in the visible region can also be achieved in the nanoshell geometry of a semiconductor material.

**ABSTRACT** We have systematically investigated the geometrically tunable optical properties of cuprous oxide (Cu<sub>2</sub>O) in a nanoshell geometry. Spherically symmetric Cu<sub>2</sub>O nanoshells with fine-controlled shell thicknesses and overall dimensions over a broad size range have been fabricated in a highly controllable manner through an Ostwald ripening-based symmetric hollowing process at room temperature. Symmetric hollowing of Cu<sub>2</sub>O particles can be achieved by using polyvinylpyrrolidone as a structural directing agent to mediate aggregation of the nuclei into solid spheres at the initial stage of the process, whereas when using other structural directing agents, such as polyethylene glycol, an asymmetric hollowing process takes place during Ostwald ripening, which gives rise to the formation of asymmetric Cu<sub>2</sub>O nanoshell structures. We demonstrate, both experimentally and theoretically, that the optical responses of Cu<sub>2</sub>O nanoshells can be fine-tuned in the visible spectral region by tailoring the inner and outer radii of the spherically symmetric nanoshells. Such optical tunability of Cu<sub>2</sub>O achieved in this nanoshell geometry is believed to be important to the optimization of Cu<sub>2</sub>O-based photonic materials and devices for photovoltaic and photocatalytic applications.

**KEYWORDS:** cuprous oxide · nanoshell · structure–property relationship · Ostwald ripening · semiconductor · photovoltaics · photocatalysis

Cuprous oxide (Cu<sub>2</sub>O), an important p-type semiconductor with interesting excitonic features,<sup>17–23</sup> has a high optical absorption coefficient and a bulk band gap of 2.2 eV, which make it an excellent candidate for applications in solar energy photovoltaics<sup>24–27</sup> and photocatalysis.<sup>28–30</sup> Upon photoexcitation, excitons in Cu<sub>2</sub>O are long-lived with typical lifetimes of ~10 microseconds, and there is already evidence to prove that the exciton motion inside solid Cu<sub>2</sub>O materials can be coherent,<sup>18,19</sup> in a manner analogous to photon coherence in lasers. Rationally tuning the optical properties of Cu<sub>2</sub>O, which can in principle be achieved through the fine-control over the dimensions and morphologies of Cu<sub>2</sub>O nanostructures, is directly related to our abilities to optimize Cu<sub>2</sub>O-based photonic materials and/or devices for next-generation photovoltaics and photocatalysis. This has, in turn, stimulated immense efforts in the development of a series of “bottom-up” approaches to the fabrication of Cu<sub>2</sub>O

\* Address correspondence to wang.hui@chem.sc.edu.

Received for review January 30, 2011  
and accepted February 25, 2011.

Published online February 25, 2011  
10.1021/nn200386n

© 2011 American Chemical Society

nanostructures with well-defined morphologies, such as spheres,<sup>31–33</sup> wires,<sup>34</sup> cubes,<sup>35,36</sup> polyhedra,<sup>37,38</sup> and hollow structures.<sup>39–46</sup> Among these nanostructures, hollow nanostructures, or nanoshells, are of particular interest because of their unique surface chemistries and structure-dependent optical properties. Although several methods involving templating or template-free processes have been developed for the fabrication of Cu<sub>2</sub>O hollow nanostructures,<sup>39–46</sup> development of detailed, quantitative understanding on the structure–property relationship of Cu<sub>2</sub>O in the nanoshell geometry has still remained a significant challenge due to lack of methods for the precise control over the inner and outer dimensions of the nanoshells.

The approach we utilized to fine-control the inner and outer dimensions and thereby to fine-tune the optical properties of Cu<sub>2</sub>O nanoshells is based on a controllable Ostwald ripening process at room temperature. Ostwald ripening, which has been commonly observed in crystal growth for more than a century, involves the growth of larger crystals from those of smaller sizes which have a higher solubility than the larger ones.<sup>47,48</sup> During a typical Ostwald ripening process, smaller crystallites gradually dissolve into solution and then recrystallize into larger ones through a multistep solid–solution–solid process, shifting the equilibrium toward the crystalline structures that are thermodynamically more stable. Interestingly, this century-old ripening phenomenon has been recently employed to fabricate novel nanoshell structures of various metal oxides and chalcogenides, such as TiO<sub>2</sub>,<sup>49</sup> SnO<sub>2</sub>,<sup>8</sup> Fe<sub>3</sub>O<sub>4</sub>,<sup>50</sup> Co<sub>3</sub>O<sub>4</sub>,<sup>51</sup> CdMoO<sub>4</sub>,<sup>52</sup> and ZnS,<sup>51</sup> under hydrothermal or solvothermal conditions at relatively high temperatures (140–220 °C) over time periods ranging from a few hours to a few days. Under our experimental conditions, the Ostwald ripening of Cu<sub>2</sub>O occurs at room temperature under ambient air through which solid Cu<sub>2</sub>O nanospheres are gradually converted into thick nanoshells, thin nanoshells, and eventually collapsed shell structures over a time period of ~2 h.

## RESULTS AND DISCUSSION

### Symmetric Hollowing of Cu<sub>2</sub>O Particles during Ostwald Ripening

**Ripening.** Figure 1 schematically illustrates the structural evolution of Cu<sub>2</sub>O particles under our experimental conditions during the Ostwald ripening process. The first step involves the assembly of Cu<sub>2</sub>O nuclei, which are formed through the reduction of Cu<sup>2+</sup> ions by hydrazine, into solid spherical aggregates. This is a kinetically fast step resulting in the formation of metastable spherical aggregates composed of a large number of small crystallites and likely amorphous domains as well. The crystallites or amorphous domains located in the inner cores usually have higher surface energies and are thus easier dissolved than

those in the outer shells essentially due to the higher curvature that a smaller sphere possesses. As a consequence, some interior cavities will be generated within the solid spheres during Ostwald ripening as larger crystallites are essentially immobile while the smaller ones are undergoing mass transport through the dissolving and recrystallization processes. We found that symmetric hollowing of Cu<sub>2</sub>O particles could be achieved by using polyvinylpyrrolidone (PVP) as a structural directing agent to mediate aggregation of the nuclei into solid spheres at the initial stage of the Ostwald ripening. As schematically illustrated in Figure 1, during the symmetric hollowing process, the shell thickness progressively decreases as the Ostwald ripening continues until shell structure begins to collapse eventually.

We have performed transmission electron microscopy (TEM) measurements to track the structural evolution of the Cu<sub>2</sub>O particles during the Ostwald ripening process. Figure 2 shows a set of TEM images that reveal the morphologies of spherical Cu<sub>2</sub>O particles (average outer radius of ~210 nm) obtained at different reaction times. It is apparent that the whole process started from spherical aggregates with solid interior structures. During Ostwald ripening, the Cu<sub>2</sub>O particles became hollow inside as the crystallites or amorphous domains in the inner cores gradually dissolved and recrystallized into larger, better crystallized domains in the outer shells, which resulted in the mass transport from inner core to outer shell space. The shell thickness of Cu<sub>2</sub>O naoshells was observed to decrease progressively as the Ostwald ripening proceeded until the shell structures eventually collapsed when a thin-shell limit was reached after ~120 min. Cu<sub>2</sub>O nanoshells with precisely controlled shell thicknesses could be obtained at different reaction times while the spherical overall morphology and outer dimension of the Cu<sub>2</sub>O nanoshells remained the same. This clearly verified that the particles underwent an inside-out symmetric hollowing process during Ostwald ripening under current experimental conditions. The evolution of the outer radii and the aspect ratios between inner and outer radii of Cu<sub>2</sub>O nanoshells as a function of reaction time are plotted in Figure S1 in the Supporting Information.

The Ostwald ripening of Cu<sub>2</sub>O particles under the current experimental conditions was observed to be a continuous process; however, once the particles were separated from the reaction mixture through centrifugation and redispersion in ethanol, the Ostwald ripening process could be effectively inhibited. This provided a way that we could stop the Ostwald ripening process at any time spot during the whole process to obtain Cu<sub>2</sub>O nanoshells with fine-controlled shell thicknesses. No measurable change in the structures or compositions of Cu<sub>2</sub>O nanoshells was observed over time periods of several months if the particles were

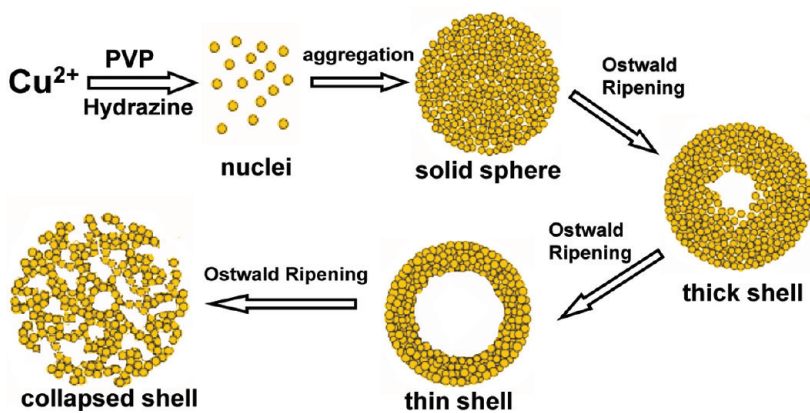


Figure 1. Schematics illustrating the symmetric hollowing of  $\text{Cu}_2\text{O}$  spherical particles in the presence of polyvinylpyrrolidone (PVP) during the Ostwald ripening process.

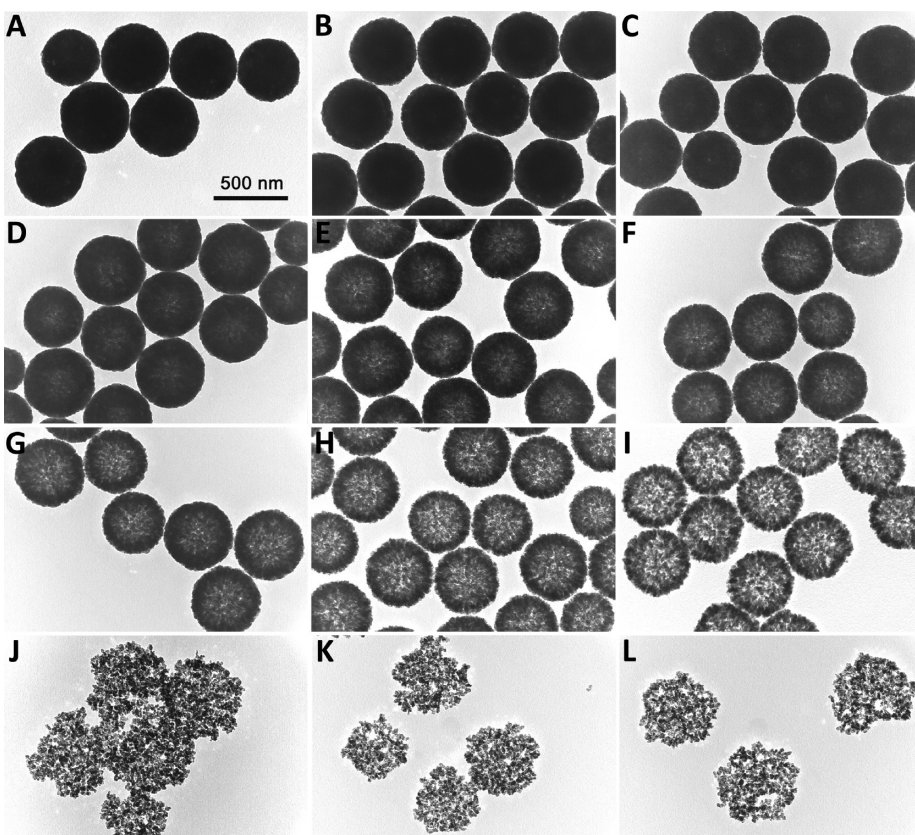
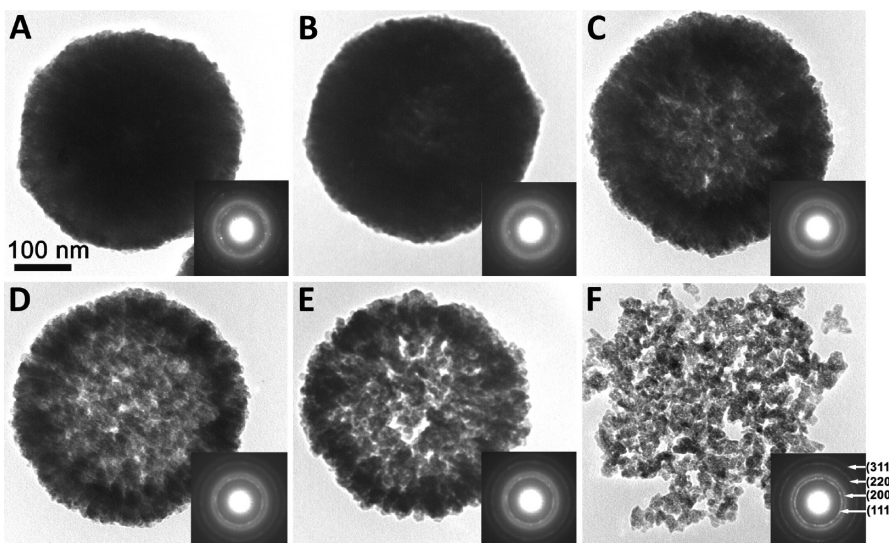


Figure 2. Symmetric hollowing of  $\text{Cu}_2\text{O}$  spherical particles in the presence of polyvinylpyrrolidone during Ostwald ripening. TEM images of  $\text{Cu}_2\text{O}$  particles obtained at different times during Ostwald ripening: (A) 5; (B) 10; (C) 15; (D) 20; (E) 30; (F) 40; (G) 50; (H) 60; (I) 90; (J) 120; (K) 150; and (L) 180 min. All the TEM images shown here share the same scale-bar in panel A.

dispersed in ethanol and stored at either room temperature or at 4 °C in refrigerator.

To correlate the morphological changes with the crystalline evolution of the nanoshells during Ostwald ripening, we have taken TEM images with higher magnifications on single particles and measured the selected area electron diffraction (SAED) of the individual particles. Figure 3 shows the TEM images and the corresponding SAED patterns taken on individual  $\text{Cu}_2\text{O}$  particles obtained at different reaction times. In the

SAED pattern of a solid sphere obtained at the initial stage of Ostwald ripening (Figure 3A), only highly diffusive and weak diffraction rings were observed, which indicated poor crystallinity of the material and small sizes of the crystallites. It was highly likely that each  $\text{Cu}_2\text{O}$  solid sphere consisted of a large number of poorly crystalline and amorphous domains. As the Ostwald ripening proceeded, the shell thickness progressively decreased while the shells became increasingly crystallized as the diffraction ring patterns



**Figure 3.** TEM images and SAED patterns (insets) of individual  $\text{Cu}_2\text{O}$  particles obtained at different reaction times during the Ostwald ripening process in the presence of polyvinylpyrrolidone: (A) 5; (B) 15; (C) 30; (D) 60; (E) 90; and (F) 120 min. All the TEM images shown here share the same scale-bar in panel A.

became brighter and better resolved in the SAED pictures (Figure 3B–E). From the high-magnification TEM images, it was obvious that each  $\text{Cu}_2\text{O}$  nanoshell displayed rough inner and outer surfaces and did not have continuous single-crystalline shell structures. The nanoshells obtained at various stages during Ostwald ripening were actually composed of a large number of small crystalline domains, each of which was around 10–30 nm in size, randomly oriented and packed into a shell structure. The concentric ring structures in the SAED patterns clearly verified the polycrystalline nature of the nanoshells and the random orientation of crystallites in the shell structures. For the thin nanoshell obtained at reaction time of 90 min, the degree of crystallinity of the shell became comparable to that of the collapsed shell structures obtained at the final stage of Ostwald ripening, which turned out to be the thermodynamically stable structure under the current experimental conditions. The concentric diffraction rings from inside to outside in Figure 3F were indexed to be corresponding to the (111), (200), (220), and (311) planes of pure cubic phase of  $\text{Cu}_2\text{O}$  with lattice constant  $a = 4.258 \text{ \AA}$  (JCPDS card no. 05-0667), respectively. No SAED feature corresponding to metallic Cu or cupric oxide ( $\text{CuO}$ ) was observed throughout the Ostwald ripening process.

The symmetric hollowing of  $\text{Cu}_2\text{O}$  particles and increased crystallinity of the nanoshell structures observed here were direct consequences of an Ostwald ripening process. To obtain spherically symmetric nanoshells, the distribution of crystallite sizes and packing density inside a spherical aggregate must be concentrically symmetric to ensure the symmetric hollowing of the particles. PVP, as a surface capping agent, is believed to play a crucial role in mediating the aggregation and packing of the  $\text{Cu}_2\text{O}$  nuclei into solid

spheres; the detailed distribution of packing density inside each  $\text{Cu}_2\text{O}$  solid sphere, however, is hard to be mapped out experimentally and is beyond the scope of this paper. It has been reported that the selective adsorption of PVP on different crystalline facets of  $\text{Cu}_2\text{O}$  plays a key role in the shape-controlled growth of  $\text{Cu}_2\text{O}$  cubic and polyhedral nanoparticles.<sup>37</sup> In the present case, it is highly likely that PVP mediates the nuclei aggregation process through its physical adsorption on  $\text{Cu}_2\text{O}$  surfaces rather than forming covalent chemical interactions with  $\text{Cu}_2\text{O}$  surfaces. Fourier transform infrared (FTIR) absorption spectra in Figure S2 in Supporting Information indicate that the adsorbed PVP on  $\text{Cu}_2\text{O}$  surfaces can be effectively removed by washing the particles through multiple cycles of centrifugation and redispersion.

#### Geometrically Tunable Optical Properties of $\text{Cu}_2\text{O}$ Nanoshells.

The as-fabricated  $\text{Cu}_2\text{O}$  nanoshells exhibited highly tunable optical responses in the visible region that were sensitively dependent on their inner and outer radii. Figure 4 shows the experimentally measured extinction (absorption + scattering) spectra of  $\text{Cu}_2\text{O}$  solid spheres, nanoshells with varying shell thicknesses, and collapsed shell structures obtained at different stages during Ostwald ripening. The extinction maximum of each spectrum was normalized to unity for clear comparison. The  $\text{Cu}_2\text{O}$  solid spherical aggregates with an average outer radius of  $\sim 210 \text{ nm}$  showed multiple features in their extinction spectrum largely due to light scattering at the Mie resonances of the particles.<sup>53</sup> Such multipeaked extinction features of  $\text{Cu}_2\text{O}$  have also been previously observed in submicrometer-sized  $\text{Cu}_2\text{O}$  solid spheres, which by themselves displayed size-dependent optical responses.<sup>54</sup> It has been reported that the extinction peaks of  $\text{Cu}_2\text{O}$  solid spheres progressively blue-shifted as the particle

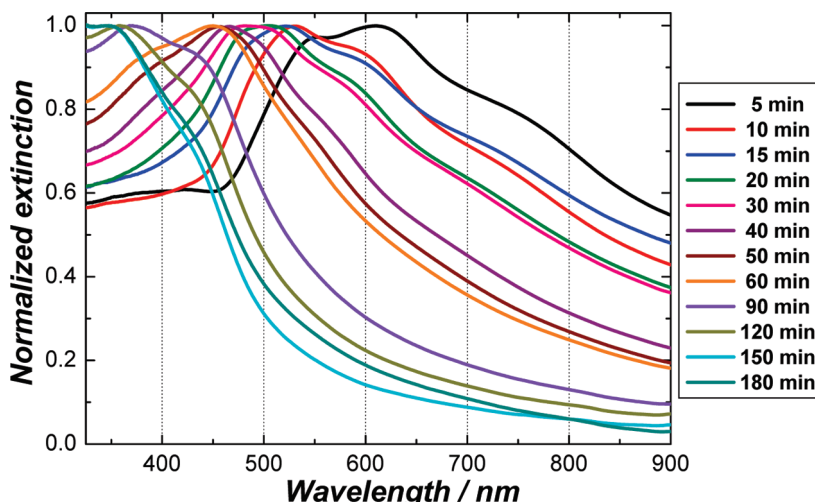


**Figure 4.** Extinction spectra of Cu<sub>2</sub>O particles obtained at different reaction times.

size decreased until an absorption edge below 400 nm became predominant in the spectra when the particles became smaller than 30 nm.<sup>54</sup> In this small particle size regime, the extinction of Cu<sub>2</sub>O is dominated by absorption rather than scattering due to the small overall particle size, and the absorption edge is attributed to the electronic interband transitions of Cu<sub>2</sub>O nanoparticles.<sup>33,55,56</sup> In the nanoshell geometry, the optical responses of Cu<sub>2</sub>O turned out to be even more sensitively dependent on the particle geometry than the solid spherical particles and could be fine-tuned all the way across the visible region by adjusting the aspect ratio between their inner and outer radii (see Figure 4). Since the outer radii of nanoshells obtained at different reaction times remained the same, the spectral evolution was directly related to the changes in the thickness of the nanoshells. As the shell thickness decreased, the spectral features in the extinction spectra progressively blue-shifted until the absorption edge below 400 nm corresponding to the Cu<sub>2</sub>O's interband transitions began to dominate the spectrum when collapsed shell structures were formed. Since the collapsed shells were primarily composed of Cu<sub>2</sub>O nanocrystals which were 15–30 nm in size (see TEM images in Figures 2J–L and Figure 3F), it was not surprising that the collapsed shells had very similar extinction spectral features as those of small Cu<sub>2</sub>O nanoparticles. The correlation between the extinction maximum wavelengths and the aspect ratio between inner and outer radii of Cu<sub>2</sub>O nanoshells is shown in Figure S1 in Supporting Information.

It is noteworthy that the spectral tunability of Cu<sub>2</sub>O nanoshells observed in the present study is essentially arising from combined contributions from the geometry-dependent light absorption and scattering by the particles rather than the quantum confinement effects. The threshold particle size for the quantum confinement effects to occur has been proposed to be in the range of sub-10 nm for Cu<sub>2</sub>O nanoparticles.<sup>33,55,56</sup> The

quantum confinement effects, which give rise to increased band gap energies in comparison to bulk materials,<sup>33,55,56</sup> may in principle also contribute to the optical tunability of Cu<sub>2</sub>O nanoshells when the shells are thinner than ~10 nm. However, the quantum confinement effects probably have no obvious contribution to the optical tunability of the Cu<sub>2</sub>O nanoshells observed here, because even for the thinnest Cu<sub>2</sub>O nanoshells one can obtain through this Ostwald ripening process, the shell thickness is still apparently thicker than 20 nm. The lack of quantum confinement effects has been further verified by photoluminescence measurements. Figure S3 in the Supporting Information shows the room-temperature photoluminescence spectra of Cu<sub>2</sub>O nanoshells obtained at different reaction times during Ostwald ripening. A series of emission peaks in the spectral range from 400 to 600 nm, which could be assigned to various band edge excitonic emissions or trapped states in defects,<sup>57</sup> were well resolved in the photoluminescence spectra under UV (190 nm) or visible (402 nm) excitation. The emission at ~548 nm could be assigned to the lowest-energy yellow excitonic emission of Cu<sub>2</sub>O corresponding to a band gap value of 2.26 eV, which is very close to the reported band gap value of Cu<sub>2</sub>O bulk materials (2.2 eV).<sup>33,55,56</sup> The photoluminescence spectra of Cu<sub>2</sub>O nanoshells with varying shell thicknesses were very similar and no blue-shift of emission peaks was observed as the shell thickness progressively decreased, indicating lack of the quantum confinement effects in these experimentally fabricated Cu<sub>2</sub>O nanoshells.

To gain further insights into the structure–property relationship, we have used Mie scattering theory (applied to concentric multilayer spherical particles)<sup>58</sup> to calculate the optical properties of Cu<sub>2</sub>O nanoshells with varying geometrical parameters. The Mie scattering theory calculation is based on an analytical solution of Maxwell's equations for the scattering and absorption of electromagnetic radiation by dielectric,

semiconductor, metallic, and composite multishell particles that are spherically symmetric.<sup>53</sup> In these calculations, we used the experimentally measured frequency-dependent, complex empirical dielectric function for bulk Cu<sub>2</sub>O,<sup>59</sup> and the dielectric medium both inside the core of nanoshells and surrounding the particles was assumed to be water (refractive index of 1.33). The calculated extinction was expressed as an efficiency, which was the ratio of the energy scattered or absorbed by the particle to the energy incident on its physical cross section.

Figure 5 shows the calculated extinction, absorption, and scattering spectra of Cu<sub>2</sub>O nanoshells with outer radius ( $R_2$ ) of 210 nm and varying inner radii ( $R_1$ ). Three major interesting trends could be clearly seen in these calculated spectra. First, the relative contribution of scattering to extinction increases in comparison to that of absorption as shell thickness increases. For Cu<sub>2</sub>O nanoshells in the thin shell regime, the extinction is dominated by absorption rather than scattering, whereas scattering dominates the extinction in the thick shell regime. Second, as shell thickness increases, higher-order multipolar resonances become increasingly pronounced in comparison to the dipolar resonances largely due to phase retardation effects,<sup>60,61</sup> giving rise to multipeaked features in the scattering and extinction spectra. Third, both the absorption edges and scattering resonance frequencies red-shift progressively as shell thickness increases. The evolution of these spectral features as shell thickness varies shown in the calculated spectra is in qualitative agreement with the experimental extinction spectra shown in Figure 4. The Mie scattering theory calculations provide a clear picture of the correlation between the particle geometry and optical properties of Cu<sub>2</sub>O nanoshells, though some discrepancies between the calculated and experimental spectra, especially for Cu<sub>2</sub>O in the thick shell regime, have also been observed largely due to the structural nonideality of the experimentally fabricated nanoshells. The geometries of Cu<sub>2</sub>O employed in the Mie theory calculations are perfectly smooth and homogeneous nanoshells; however, the as-fabricated Cu<sub>2</sub>O nanoshells are inhomogeneous and polycrystalline in nature. As shown in Figures 2 and 3, the as-fabricated nanoshells are composed of a large number of nanocrystalline domains and the size, crystallinity, orientation, and packing density of the crystallites are all factors that may introduce modifications to the dielectric function of the Cu<sub>2</sub>O nanoshells in comparison to that of the single-crystalline bulk Cu<sub>2</sub>O<sup>59</sup> which we used for these calculations. In addition, inhomogeneous broadening due to polydispersity of the Cu<sub>2</sub>O samples may further modify the overall line shape of the spectral features.

As demonstrated above, the Ostwald ripening of Cu<sub>2</sub>O under our experimental conditions provides a unique way to fine-control the shell thickness and

thereby to systematically tune the light scattering and absorption properties of Cu<sub>2</sub>O nanoshells. We have further found that this symmetric hollowing process was independent of the overall size of the Cu<sub>2</sub>O solid spheres formed at the initial stage of Ostwald ripening. We have also used the same strategy to fine-control the shell thickness of Cu<sub>2</sub>O nanoshells with varying outer radii and two examples of Cu<sub>2</sub>O nanoshells with average outer radii of ~60 and ~120 nm are shown in Figures S4 and S5 in Supporting Information, respectively. In both cases, the optical responses of Cu<sub>2</sub>O in the visible region could be fine-tuned by tailoring the shell thickness as well. Taken together, the Ostwald ripening-based symmetric hollowing process reported here provides a convenient approach to control both the inner and outer radii of Cu<sub>2</sub>O nanoshells over a broad size range, allowing the fine-tuning of the light scattering and absorption properties of Cu<sub>2</sub>O nanoshells over a broad spectral range.

**Asymmetric Hollowing of Cu<sub>2</sub>O Particles during Ostwald Ripening.** The Ostwald ripening processes discussed above all proceed in a highly symmetric and isotropic manner, which leads to the formation of spherically symmetric Cu<sub>2</sub>O nanoshells. This is essentially because variations in the crystallite size and packing densities are concentrically distributed in the respective spherical aggregates. However, if the primary crystallites are packed in an asymmetric manner in the starting aggregates, the Ostwald ripening process might be initiated somewhere other than the central point and as a result, random, anisotropic cavities will be created inside the spheres, giving rise to asymmetric hollowing of the Cu<sub>2</sub>O particles. As a proof-of-concept, we have also used polyethylene glycol (PEG) as the structural-directing agent instead of PVP, and asymmetric hollowing of Cu<sub>2</sub>O particles was indeed observed. Analogous to PVP, it is likely that PEG mediates the nuclei aggregation process also through its physical adsorption on Cu<sub>2</sub>O surfaces. FT-IR spectra in Figure S6 in Supporting Information indicate that the adsorbed PEG on Cu<sub>2</sub>O surfaces can be effectively removed by washing the particles through multiple cycles of centrifugation and redispersion. However, the distribution of crystallite sizes and packing density inside the Cu<sub>2</sub>O solid spheres at the initial stage of Ostwald ripening could be very different from those formed in the presence of PVP, giving rise to dramatically different particle hollowing processes.

Figure 6A–H show a set of TEM images that reveal the morphological evolution of Cu<sub>2</sub>O particles in the presence of PEG during Ostwald ripening. It is apparent that the structural evolution of Cu<sub>2</sub>O particles turned out to be highly heterogeneous and anisotropic and the asymmetric hollowing process gave rise to the formation of asymmetric nanoshell structures. Since Ostwald ripening was not initiated in the center of the

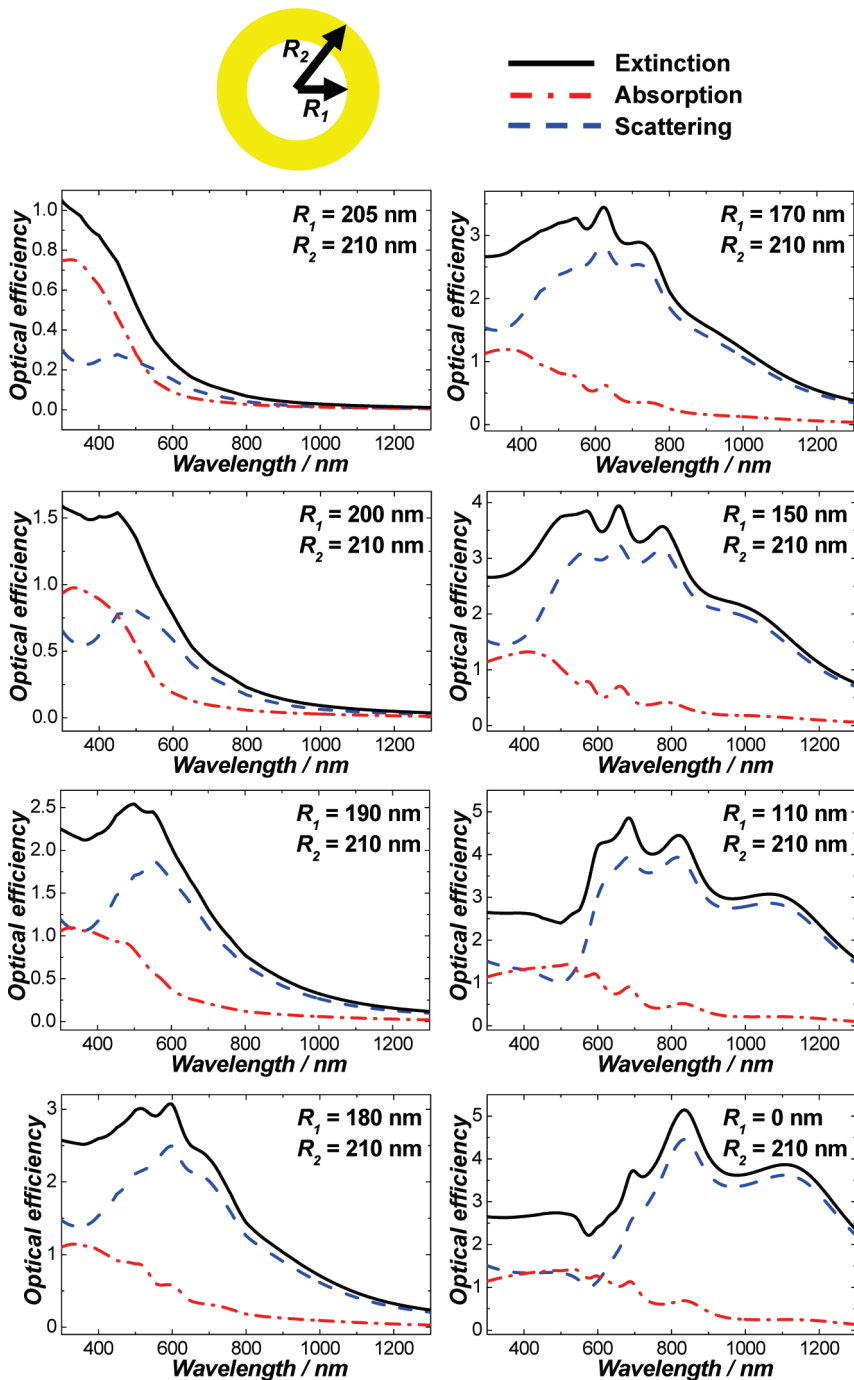
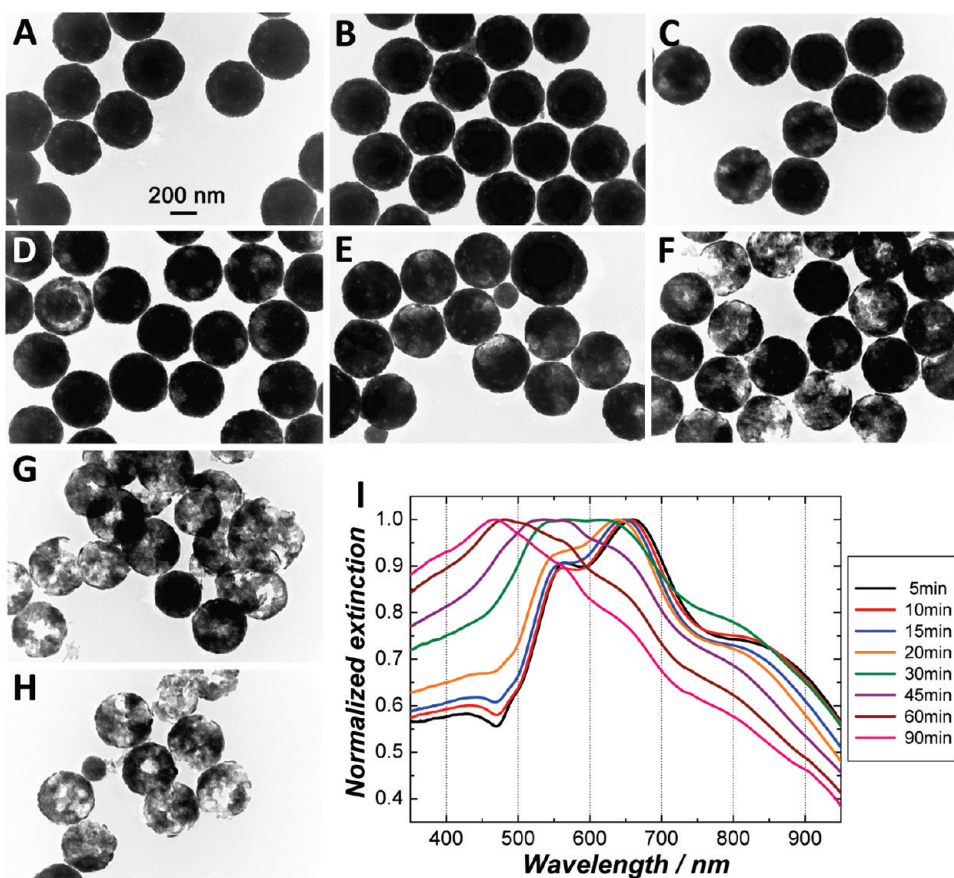


Figure 5. Calculated extinction, absorption, and scattering spectra of  $\text{Cu}_2\text{O}$  nanoshells with outer radius ( $R_2$ ) of 210 nm and varying inner radii ( $R_1$ ) as indicated in each panel.

solid spheres, some rattle-like, yolk–shell structures were also formed at some intermediate stages during the Ostwald ripening (see Figure 6B–D). Unlike the symmetric hollowing process in which the nanoshell structures collapsed all at once when the thin-shell limit was reached, the asymmetric nanoshell structures began to break at certain places on surface before complete collapse (see Figure 6F–H), giving rise to the formation of some anisotropic half-shell and partially broken nanocup structures.

It is interesting that geometrically tunable optical properties could also be achieved in these asymmetric  $\text{Cu}_2\text{O}$  nanoshell structures as shown in Figure 6I. The  $\text{Cu}_2\text{O}$  solid spheres, rattle-like core–shell structures, and asymmetrically broken shells all exhibited complicated, multipeaked features in their extinction spectra, which progressively blue-shifted as the Ostwald ripening process proceeded. In principle, the optical properties of  $\text{Cu}_2\text{O}$  can also be fine-tuned through this PEG-mediated asymmetric hollowing process; however,



**Figure 6.** Asymmetric hollowing of  $\text{Cu}_2\text{O}$  spherical particles in the presence of polyethylene glycol during Ostwald ripening. TEM images of  $\text{Cu}_2\text{O}$  particles obtained at different reaction times during Ostwald ripening: (A) 5; (B) 10; (C) 15; (D) 20; (E) 30; (F) 45; (G) 60; (H) 90 min. All the TEM images shown here share the same scale-bar in panel A. (I) Extinction spectra of the  $\text{Cu}_2\text{O}$  particles obtained at different reaction times.

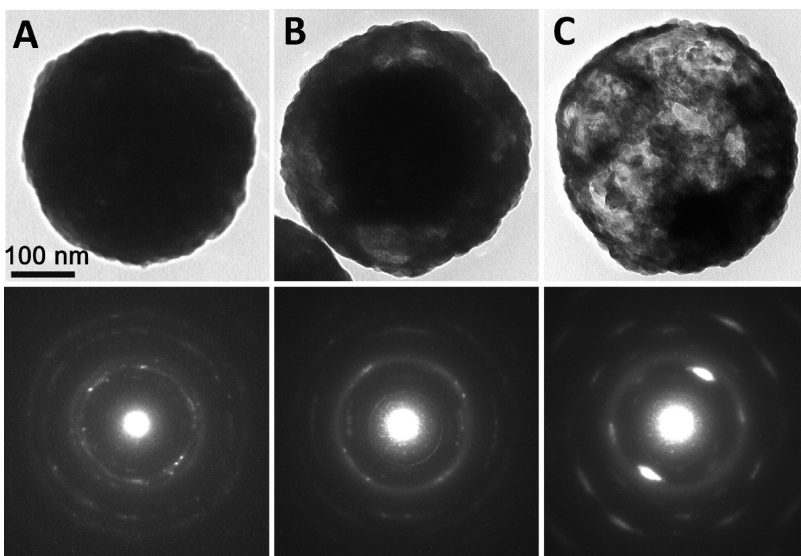


**Figure 7.** TEM images (top panels) and SAED patterns (bottom panels) of individual  $\text{Cu}_2\text{O}$  particles obtained at different reaction times during the polyethylene glycol-mediated asymmetric hollowing process: (A) 5; (B) 30; and (C) 60 min. All the TEM images shown here share the same scale-bar in panel A.

quantification of detailed correlation between the particle geometry and their optical properties turned out

to be challenging primarily due to the asymmetry, complexity, and heterogeneity of the particle structures.

Figure 7 shows the high-magnification TEM images and SAED patterns of individual Cu<sub>2</sub>O particles obtained during the PEG-mediated asymmetric hollowing process. The initial solid spherical aggregate of Cu<sub>2</sub>O was apparently polycrystalline as well-defined, continuous concentric rings were observed in the SAED pattern (Figure 7A). For a rattle-like core–shell particle obtained after 30 min, the diffraction rings in the SAED pattern (Figure 7B) became discontinuous, indicating a decreased number of single-crystalline domains in the particles as the originally smaller crystallites underwent the Ostwald ripening process to recrystallize into larger crystalline domains. For an asymmetrically broken nanoshell obtained after 60 min, only discrete diffraction spots were observed in the SAED pattern (Figure 7C), suggesting a further increased crystallinity of the shell structures as a result of Ostwald ripening.

## CONCLUSION

We have systematically investigated the optical tunability of Cu<sub>2</sub>O in a nanoshell geometry. We have

demonstrated that the optical properties of Cu<sub>2</sub>O nanoshells in the visible spectral region can be fine-tuned by tailoring the inner and outer dimensions of the nanoshells. Spherically symmetric Cu<sub>2</sub>O nanoshells with fine-controlled shell thicknesses and overall dimensions have been successfully fabricated in a highly controllable manner through an Ostwald ripening-based symmetric hollowing process. We found that symmetric hollowing could be achieved by using PVP as a structural directing agent to mediate aggregation of the nuclei into solid spheres at the initial stage of the process, whereas when using other structural directing agents, such as PEG, an asymmetric hollowing process could take place during Ostwald ripening, which gave rise to the formation of asymmetric nanoshell structures. This paper demonstrates a highly controllable approach to fine-tuning the optical properties of Cu<sub>2</sub>O nanoshells in the visible region, which is believed to be important to the optimization of Cu<sub>2</sub>O-based photonic materials and devices for photovoltaic and photocatalytic applications.

## METHODS

In a typical procedure for the fabrication of Cu<sub>2</sub>O nanoshells (average outer radius of 210 nm), 1.0 g of PVP (Alfa Aesar, average MW = 58000) was added into 50 mL of 0.02 M Cu(NO<sub>3</sub>)<sub>2</sub> (Alfa Aesar) aqueous solution under rapid magnetic stir (250 rpm). The mixture was kept stirring for several minutes until the powders were completely dissolved. Then 45.2  $\mu$ L of hydrazine solution (35 wt % N<sub>2</sub>H<sub>4</sub>, Aldrich) was added to the mixture solution dropwise. A colloidal solution of Cu<sub>2</sub>O particles which was orange in color formed immediately after the introduction of N<sub>2</sub>H<sub>4</sub> within  $\sim$ 15 s. The resulting colloidal solution was kept stirring under ambient air for Ostwald ripening, and the color of the Cu<sub>2</sub>O colloids was observed to change from orange to light yellow gradually over a time period of  $\sim$ 2 h, indicating structural changes of the Cu<sub>2</sub>O particles. All experiments were carried out at room temperature, and ultrapure water (18.2 M $\Omega$  resistivity, Barnstead EasyPure II 7138) was used. During the Ostwald ripening process, we typically withdrew aliquots of colloidal solutions at certain reaction times from the reaction mixture, then immediately centrifuged the particles, washed them three times with water and ethanol, and finally dispersed them in ethanol. The samples were stored either at room temperature or at 4 °C in refrigerator.

The outer radii of Cu<sub>2</sub>O nanoshells could be controlled by adjusting the initial concentration of Cu<sup>2+</sup>. We found that the average outer radii of as-fabricated Cu<sub>2</sub>O nanoshells decreased as the Cu<sup>2+</sup> concentration increased when the starting concentration of Cu<sup>2+</sup> was in the range of 0.02–0.2 M. To fabricate Cu<sub>2</sub>O nanoshells with average outer radii of 60 nm, 0.1 M Cu(NO<sub>3</sub>)<sub>2</sub> and 226  $\mu$ L of 35 wt % N<sub>2</sub>H<sub>4</sub> solution were introduced into the reaction mixture while all the other experimental conditions were exactly the same. To fabricate Cu<sub>2</sub>O nanoshells with average outer radii of 120 nm, 0.05 M Cu(NO<sub>3</sub>)<sub>2</sub> and 113  $\mu$ L of 35 wt % N<sub>2</sub>H<sub>4</sub> solution were introduced into the reaction mixture while all the other experimental conditions were kept the same.

The asymmetric Cu<sub>2</sub>O nanoshells were fabricated through the PEG-mediated Ostwald ripening process in which PEG was introduced instead of PVP while keeping the other experimental conditions unchanged. Briefly, 0.6 g of PEG (Aldrich, average

MW = 5000) was added into 50 mL of 0.02 M Cu(NO<sub>3</sub>)<sub>2</sub> aqueous solution under rapid magnetic stir (250 rpm). After the powders were completely dissolved, 45.2  $\mu$ L of 35 wt % N<sub>2</sub>H<sub>4</sub> was introduced into the mixture solution dropwise and the reaction mixture was kept stirring under ambient air for Ostwald ripening to obtain the rattle-like, yolk–shell structures and asymmetrically broken nanoshell structures of Cu<sub>2</sub>O.

TEM and SAED images were taken using a Hitachi H-8000 transmission electron microscope. The extinction spectra of Cu<sub>2</sub>O nanoparticles (colloidal solutions dispersed in water) were measured using a Beckman coulter Du 640 spectrophotometer at room temperature. Photoluminescence measurements were performed on aqueous suspension of Cu<sub>2</sub>O particles at room temperature using a Varian Cary Eclipse Scanning Fluorescence Spectrophotometer. FT-IR spectra were obtained using a Shimadzu 8400 FT-IR spectrometer.

**Acknowledgment.** This work was supported by the Start-up Funds provided by University of South Carolina. H. Wang would like to thank Naomi J. Halas of Rice University for providing the access to the Mie scattering theory-based “ASHELL” program (written in C++) for the calculation of nanoparticle optical properties. The authors would also like to acknowledge Qian Wang and John Lavigne of University of South Carolina for providing the access to their facilities for photoluminescence and extinction spectroscopic measurements.

**Supporting Information Available:** Figure S1, wavelength of extinction maxima, ratio between inner and outer radii ( $R_1/R_2$ ), and outer radii ( $R_2$ ) of the Cu<sub>2</sub>O particles obtained at different reaction times during the PVP-mediated Ostwald ripening process; Figure S2, FT-IR spectra of pure PVP and Cu<sub>2</sub>O particles obtained at different reaction times during the PVP-mediated Ostwald ripening process; Figure S3, photoluminescence spectra of Cu<sub>2</sub>O nanoshells obtained at different reaction times during the PVP-mediated Ostwald ripening process; Figure S4, symmetric hollowing of Cu<sub>2</sub>O spherical particles with average outer radius of  $\sim$ 60 nm in the presence of PVP during Ostwald ripening; Figure S5, symmetric hollowing of Cu<sub>2</sub>O spherical particles with average outer radius of  $\sim$ 120 nm in the presence of PVP during Ostwald ripening; Figure S6, FT-IR spectra of pure

PEG and Cu<sub>2</sub>O particles obtained at different reaction times during the PEG-mediated Ostwald ripening process. This material is available free of charge via the Internet at <http://pubs.acs.org>.

## REFERENCES AND NOTES

- Li, J.; Zeng, H. C. Nanoreactors—Size Tuning, Functionalization, and Reactivation of Au in TiO<sub>2</sub> Nanoreactors. *Angew. Chem., Int. Ed.* **2005**, *44*, 4342–4345.
- Lee, J.; Park, J. C.; Song, H. A Nanoreactor Framework of a Au@SiO<sub>2</sub> Yolk/Shell Structure for Catalytic Reduction of *p*-Nitrophenol. *Adv. Mater.* **2008**, *20*, 1523–1528.
- Yin, Y. D.; Rioux, R. M.; Erdonmez, C. K.; Hughes, S.; Somorjai, G. A.; Alivisatos, A. P. Formation of Hollow Nanocrystals through the Nanoscale Kirkendall Effect. *Science* **2004**, *304*, 711–714.
- Kim, S. W.; Kim, M.; Lee, W. Y.; Hyeon, T. Fabrication of Hollow Palladium Spheres and Their Successful Application to the Recyclable Heterogeneous Catalyst for Suzuki Coupling Reactions. *J. Am. Chem. Soc.* **2002**, *124*, 7642–7643.
- Zhu, Y. F.; Shi, J. L.; Shen, W. H.; Dong, X. P.; Feng, J. W.; Ruan, M. L.; Li, Y. S. Stimuli-Responsive Controlled Drug Release from a Hollow Mesoporous Silica Sphere/Polyelectrolyte Multilayer Core–Shell Structure. *Angew. Chem., Int. Ed.* **2005**, *44*, 5083–5087.
- Liu, J.; Qiao, S. Z.; Hartono, S. B.; Lu, G. Q. Monodisperse Yolk–Shell Nanoparticles with a Hierarchical Porous Structure for Delivery Vehicles and Nanoreactors. *Angew. Chem., Int. Ed.* **2010**, *49*, 4981–4985.
- Lee, K. T.; Jung, Y. S.; Oh, S. M. Synthesis of Tin-Encapsulated Spherical Hollow Carbon for Anode Material in Lithium Secondary Batteries. *J. Am. Chem. Soc.* **2003**, *125*, 5652–5653.
- Lou, X. W.; Wang, Y.; Yuan, C. L.; Lee, J. Y.; Archer, L. A. Template-free Synthesis of SnO<sub>2</sub> Hollow Nanostructures with High Lithium Storage Capacity. *Adv. Mater.* **2006**, *18*, 2325–2329.
- Hirsch, L. R.; Stafford, R. J.; Bankson, J. A.; Sershen, S. R.; Rivera, B.; Price, R. E.; Hazle, J. D.; Halas, N. J.; West, J. L. Nanoshell-Mediated Near-Infrared Thermal Therapy of Tumors under Magnetic Resonance Guidance. *Proc. Natl. Acad. Sci. U.S.A.* **2003**, *100*, 13549–13554.
- Chen, J. Y.; Wang, D. L.; Xi, J. F.; Au, L.; Siekkinen, A.; Warsen, A.; Li, Z. Y.; Zhang, H.; Xia, Y. N.; Li, X. D. Immuno Gold Nanocages with Tailored Optical Properties for Targeted Photothermal Destruction of Cancer Cells. *Nano Lett.* **2007**, *7*, 1318–1322.
- Oldenburg, S. J.; Averitt, R. D.; Westcott, S. L.; Halas, N. J. Nanoengineering of Optical Resonances. *Chem. Phys. Lett.* **1998**, *288*, 243–247.
- Sun, Y. G.; Xia, Y. N. Increased Sensitivity of Surface Plasmon Resonance of Gold Nanoshells Compared to that of Gold Solid Colloids in Response to Environmental Changes. *Anal. Chem.* **2002**, *74*, 5297–5305.
- Jackson, J. B.; Halas, N. J. Silver Nanoshells: Variations in Morphologies and Optical Properties. *J. Phys. Chem. B* **2001**, *105*, 2743–2746.
- Wang, H.; Tam, F.; Grady, N. K.; Halas, N. J. Cu Nanoshells: Effects of Interband Transitions on the Nanoparticle Plasmon Resonance. *J. Phys. Chem. B* **2005**, *109*, 18218–18222.
- Prodan, E.; Radloff, C.; Halas, N. J.; Nordlander, P. A Hybridization Model for the Plasmon Response of Complex Nanostructures. *Science* **2003**, *302*, 419–422.
- Wang, H.; Brandl, D. W.; Nordlander, P.; Halas, N. J. Plasmonic Nanostructures: Artificial Molecules. *Acc. Chem. Res.* **2007**, *40*, 53–62.
- Snoke, D.; Wolfe, J. P.; Mysyrowicz, A. Quantum Saturation of a Bose-Gas—Excitons in Cu<sub>2</sub>O. *Phys. Rev. Lett.* **1987**, *59*, 827–830.
- Snoke, D. Coherent Exciton Waves. *Science* **1996**, *273*, 1351–1352.
- Snoke, D. Spontaneous Bose Coherence of Excitons and Polaritons. *Science* **2002**, *298*, 1368–1372.
- Jolk, A.; Klingshirn, C. F. Linear and Nonlinear Excitonic Absorption and Photoluminescence Spectra in Cu<sub>2</sub>O: Line Shape Analysis and Exciton Drift. *Phys. Status Solidi B* **1998**, *206*, 841–850.
- Matsumoto, H.; Saito, K.; Hasuo, M.; Kono, S.; Nagasawa, N. Revived Interest on Yellow-Exciton Series in Cu<sub>2</sub>O: An Experimental Aspect. *Solid State Commun.* **1996**, *97*, 125–129.
- Ettema, A.; Versluis, J. Dipole-Allowed Generation of the Yellow-Series Excitons in Cu<sub>2</sub>O Due to an Applied Electric Field. *Phys. Rev. B* **2003**, *68*, 235101.
- Karpinska, K.; Mostovoy, M.; van der Vegt, M. A.; Revcolevschi, A.; van Loosdrecht, P. H. M. Decay and Coherence of Two-Photon Excited Yellow Orthoexcitons in Cu<sub>2</sub>O. *Phys. Rev. B* **2005**, *72*, 155201.
- Briskman, R. N. A Study of Electrodeposited Cuprous-Oxide Photovoltaic Cells. *Sol. Energy Mater. Sol. Cells* **1992**, *27*, 361–368.
- Musa, A. O.; Akomolafe, T.; Carter, M. J. Production of Cuprous Oxide, a Solar Cell Material, by Thermal Oxidation and a Study of Its Physical and Electrical Properties. *Sol. Energy Mater. Sol. Cells* **1998**, *51*, 305–316.
- Olsen, L. C.; Addis, F. W.; Miller, W. Experimental and Theoretical Studies of Cu<sub>2</sub>O Solar-Cells. *Sol. Cells* **1982**, *7*, 247–279.
- Rai, B. P. Cu<sub>2</sub>O Solar-Cells—A Review. *Sol. Cells* **1988**, *25*, 265–272.
- de Jongh, P. E.; Vanmaekelbergh, D.; Kelly, J. J. Cu<sub>2</sub>O: A Catalyst for the Photochemical Decomposition of Water?. *Chem. Commun.* **1999**, 1069–1070.
- Hara, M.; Kondo, T.; Komoda, M.; Ikeda, S.; Shinohara, K.; Tanaka, A.; Kondo, J. N.; Domen, K. Cu<sub>2</sub>O as a Photocatalyst for Overall Water Splitting under Visible Light Irradiation. *Chem. Commun.* **1998**, 357–358.
- Xu, L.; Jiang, L. P.; Zhu, J. J. Sonochemical Synthesis and Photocatalysis of Porous Cu<sub>2</sub>O Nanospheres with Controllable Structures. *Nanotechnology* **2009**, *20*, 045605.
- Zhang, J. T.; Liu, J. F.; Peng, Q.; Wang, X.; Li, Y. D. Nearly Monodisperse Cu<sub>2</sub>O and CuO Nanospheres: Preparation and Applications for Sensitive Gas Sensors. *Chem. Mater.* **2006**, *18*, 867–871.
- Pang, M. L.; Zeng, H. C. Highly Ordered Self-Assemblies of Submicrometer Cu<sub>2</sub>O Spheres and Their Hollow Chalcogenide Derivatives. *Langmuir* **2010**, *26*, 5963–5970.
- Yin, M.; Wu, C. K.; Lou, Y. B.; Burda, C.; Koberstein, J. T.; Zhu, Y. M.; O'Brien, S. Copper Oxide Nanocrystals. *J. Am. Chem. Soc.* **2005**, *127*, 9506–9511.
- Wang, W. Z.; Wang, G. H.; Wang, X. S.; Zhan, Y. J.; Liu, Y. K.; Zheng, C. L. Synthesis and Characterization of Cu<sub>2</sub>O Nanowires by a Novel Reduction Route. *Adv. Mater.* **2002**, *14*, 67–69.
- Gou, L. F.; Murphy, C. J. Solution-Phase Synthesis of Cu<sub>2</sub>O Nanocubes. *Nano Lett.* **2003**, *3*, 231–234.
- Kuo, C. H.; Chen, C. H.; Huang, M. H. Seed-Mediated Synthesis of Monodispersed Cu<sub>2</sub>O Nanocubes with Five Different Size Ranges from 40 to 420 nm. *Adv. Funct. Mater.* **2007**, *17*, 3773–3780.
- Zhang, D. F.; Zhang, H.; Guo, L.; Zheng, K.; Han, X. D.; Zhang, Z. Delicate Control of Crystallographic Facet-Oriented Cu<sub>2</sub>O Nanocrystals and the Correlated Adsorption Ability. *J. Mater. Chem.* **2009**, *19*, 5220–5225.
- Kuo, C. H.; Huang, M. H. Morphologically Controlled Synthesis of Cu<sub>2</sub>O Nanocrystals and their Properties. *Nano Today* **2010**, *5*, 106–116.
- Cao, Y. B.; Fan, J. M.; Bai, L. Y.; Yuan, F. L.; Chen, Y. F. Morphology Evolution of Cu<sub>2</sub>O from Octahedra to Hollow Structures. *Cryst. Growth Des.* **2010**, *10*, 232–236.
- Xu, H. L.; Wang, W. Z. Template Synthesis of Multi-shelled Cu<sub>2</sub>O Hollow Spheres with a Single-Crystalline Shell Wall. *Angew. Chem., Int. Ed.* **2007**, *46*, 1489–1492.
- Chang, Y.; Teo, J. J.; Zeng, H. C. Formation of Colloidal CuO Nanocrystallites and their Spherical Aggregation and Reductive Transformation to Hollow Cu<sub>2</sub>O Nanospheres. *Langmuir* **2005**, *21*, 1074–1079.

42. Teo, J. J.; Chang, Y.; Zeng, H. C. Fabrications of Hollow Nanocubes of  $\text{Cu}_2\text{O}$  and Cu via Reductive Self-Assembly of CuO Nanocrystals. *Langmuir* **2006**, *22*, 7369–7377.
43. Lu, C. H.; Qi, L. M.; Yang, J. H.; Wang, X. Y.; Zhang, D. Y.; Xie, J. L.; Ma, J. M. One-Pot Synthesis of Octahedral  $\text{Cu}_2\text{O}$  Nanocages via a Catalytic Solution Route. *Adv. Mater.* **2005**, *17*, 2562–2567.
44. Gao, J. N.; Li, Q. S.; Zhao, H. B.; Li, L. S.; Liu, C. L.; Gong, Q. H.; Qi, L. M. One-Pot Synthesis of Uniform  $\text{Cu}_2\text{O}$  and CuS Hollow Spheres and Their Optical Limiting Properties. *Chem. Mater.* **2008**, *20*, 6263–6269.
45. Zhu, H. T.; Wang, J. X.; Xu, G. Y. Fast Synthesis of  $\text{Cu}_2\text{O}$  Hollow Microspheres and Their Application in DNA Biosensor of Hepatitis B Virus. *Cryst. Growth Des.* **2009**, *9*, 633–638.
46. Hung, L. I.; Tsung, C. K.; Huang, W. Y.; Yang, P. D. Room-Temperature Formation of Hollow  $\text{Cu}_2\text{O}$  Nanoparticles. *Adv. Mater.* **2010**, *22*, 1910–1914.
47. Ostwald, W. Studien über die Bildung und Umwandlung fester Körper. *Z. Phys. Chem.* **1897**, *22*, 289.
48. McNaught, A. D.; Wilkinson, A. *IUPAC Compendium of Chemical Terminology*, (the “Gold Book”), 2nd ed.; Blackwell Scientific Publications: Oxford, 1997.
49. Yang, H. G.; Zeng, H. C. Preparation of Hollow Anatase  $\text{TiO}_2$  Nanospheres via Ostwald Ripening. *J. Phys. Chem. B* **2004**, *108*, 3492–3495.
50. Yu, D. B.; Sun, X. Q.; Zou, J. W.; Wang, Z. R.; Wang, F.; Tang, K. Oriented Assembly of  $\text{Fe}_3\text{O}_4$  Nanoparticles into Monodisperse Hollow Single-crystal Microspheres. *J. Phys. Chem. B* **2006**, *110*, 21667–21671.
51. Liu, B.; Zeng, H. C. Symmetric and Asymmetric Ostwald Ripening in the Fabrication of Homogeneous Core–Shell Semiconductors. *Small* **2005**, *1*, 566–571.
52. Wang, W. S.; Zhen, L.; Xu, C. Y.; Zhang, B. Y.; Shao, W. Z. Room Temperature Synthesis of Hollow  $\text{CdMoO}_4$  Microspheres by a Surfactant-free Aqueous Solution Route. *J. Phys. Chem. B* **2006**, *110*, 23154–23158.
53. Bohren, C. F.; Huffman, D. R. *Absorption and Scattering of Light by Small Particles*; Wiley: New York, 1983.
54. Bardhan, R.; Grady, N. K.; Ali, T.; Halas, N. J. Metallic Nano-shells with Semiconductor Cores: Optical Characteristics Modified by Core Medium Properties. *ACS Nano* **2010**, *4*, 6169–6179.
55. Borgohain, K.; Murase, N.; Mahamuni, S. Synthesis and Properties of  $\text{Cu}_2\text{O}$  Quantum Particles. *J. Appl. Phys.* **2002**, *92*, 1292–1297.
56. Deki, S.; Akamatsu, K.; Yano, T.; Mizuhata, M.; Kajinami, A. Preparation and Characterization of Copper(I) Oxide Nanoparticles Dispersed in a Polymer Matrix. *J. Mater. Chem.* **1998**, *8*, 1865–1868.
57. Yang, Z.; Chang, C. K.; Chang, H. T. Synthesis of Fluorescent and Photovoltaic  $\text{Cu}_2\text{O}$  Nanocubes. *Nanotechnology* **2008**, *19*, 025604.
58. Aden, A. L.; Kerker, M. Scattering of Electromagnetic Waves from Two Concentric Spheres. *J. Appl. Phys.* **1951**, *22*, 1242–1246.
59. Ribbing, C. G.; Roos, A. Copper Oxides ( $\text{Cu}_2\text{O}$ , CuO). In *Handbook of Optical Constants of Solids*, Palik, E. D., Ed. Academic Press: San Diego, 1991; Vol. 2, pp 875–882.
60. Westcott, S. L.; Jackson, J. B.; Radloff, C.; Halas, N. J. Relative Contributions to the Plasmon Line Shape of Metal Nano-shells. *Phys. Rev. B* **2002**, *66*, 155431.
61. Wang, H.; Halas, N. J. Mesoscopic Au “Meatball” Particles. *Adv. Mater.* **2008**, *20*, 820–825.

## **Supporting Information**

# **Cuprous Oxide Nanoshells with Geometrically Tunable Optical Properties**

*Li Zhang and Hui Wang \**

*Department of Chemistry and Biochemistry, University of South Carolina, Columbia, SC 29208*

\* To whom correspondence should be addressed. Email: [wang.hui@chem.sc.edu](mailto:wang.hui@chem.sc.edu);  
Phone: 1-803-777-2203; Fax: 1-803-777-9521.

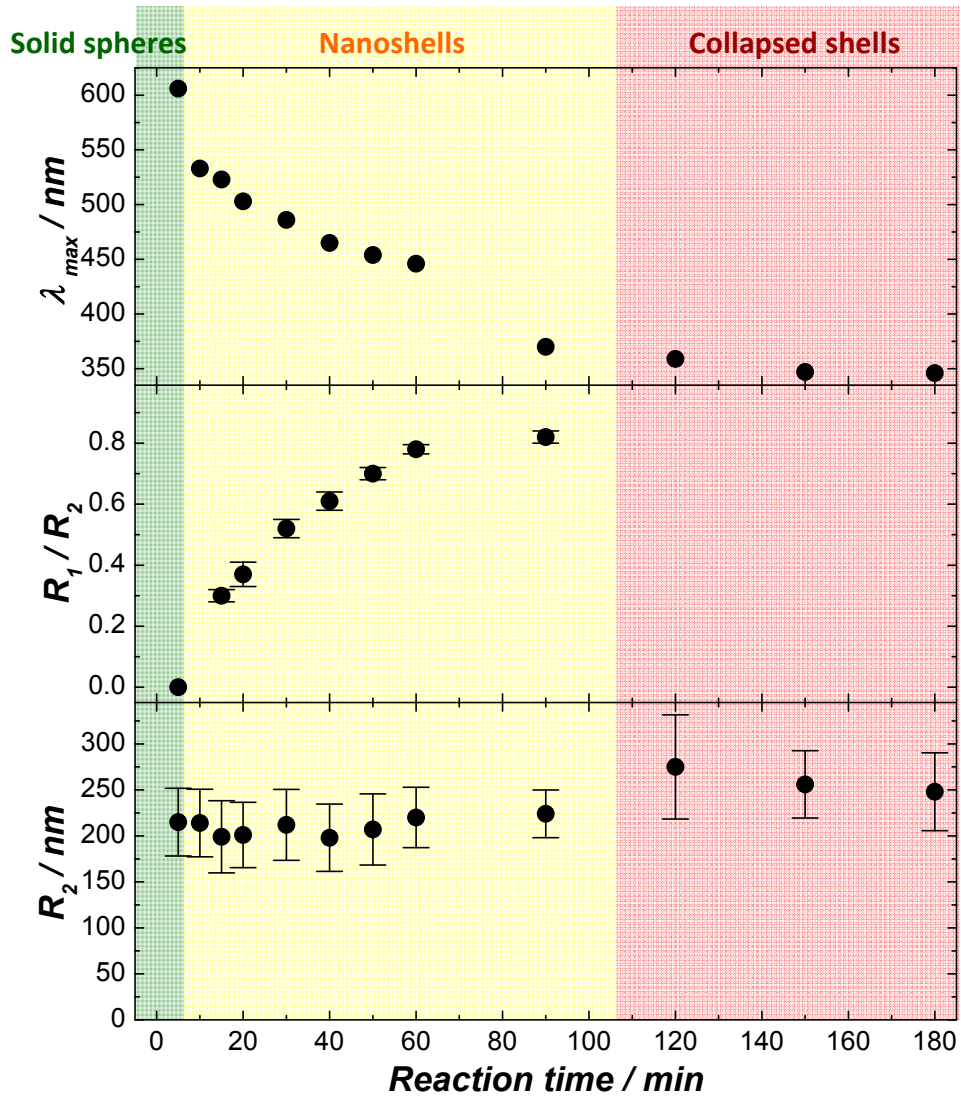


**Figure S1.** (top panel) Wavelength of the maxima in extinction spectra, (middle panel) ratio between inner and outer radii ( $R_1/R_2$ ), and (bottom panel) outer radii ( $R_2$ ) of the  $\text{Cu}_2\text{O}$  particles obtained at different reaction times during the Ostwald ripening process.  $R_1$  and  $R_2$  values were determined by TEM measurements. The error bars for  $R_1/R_2$  in the middle panel represent the standard deviations obtained from  $\sim 50$  particles and the error bars for  $R_2$  in the bottom panel represent the standard deviation obtained from  $\sim 300$  particles.

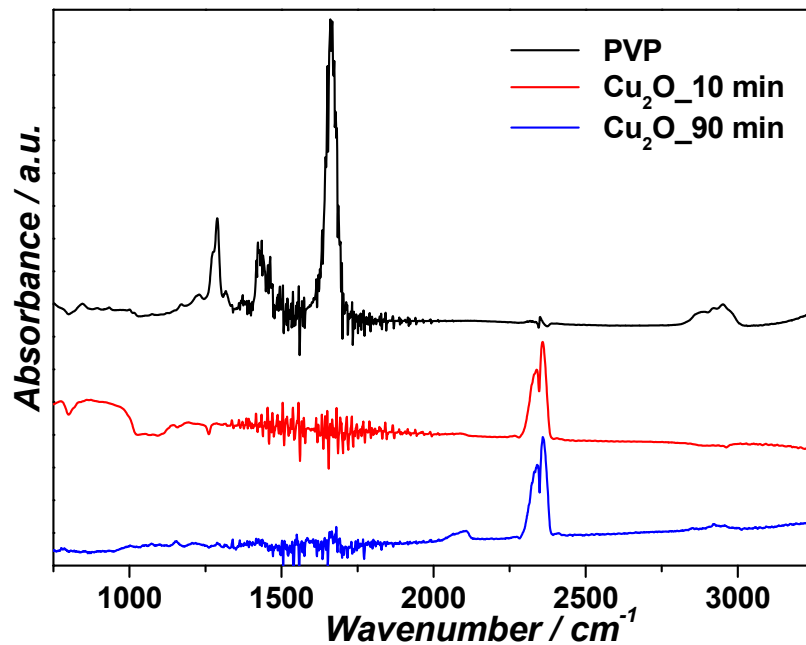


**Figure S2.** FT-IR spectra of pure PVP and Cu<sub>2</sub>O particles obtained at 10 minutes and 90 minutes during the PVP-mediated Ostwald ripening process. The double-peaked feature at 2360 cm<sup>-1</sup> and 2335 cm<sup>-1</sup> is corresponding to the CO<sub>2</sub> adsorbed on the surface of Cu<sub>2</sub>O particles.

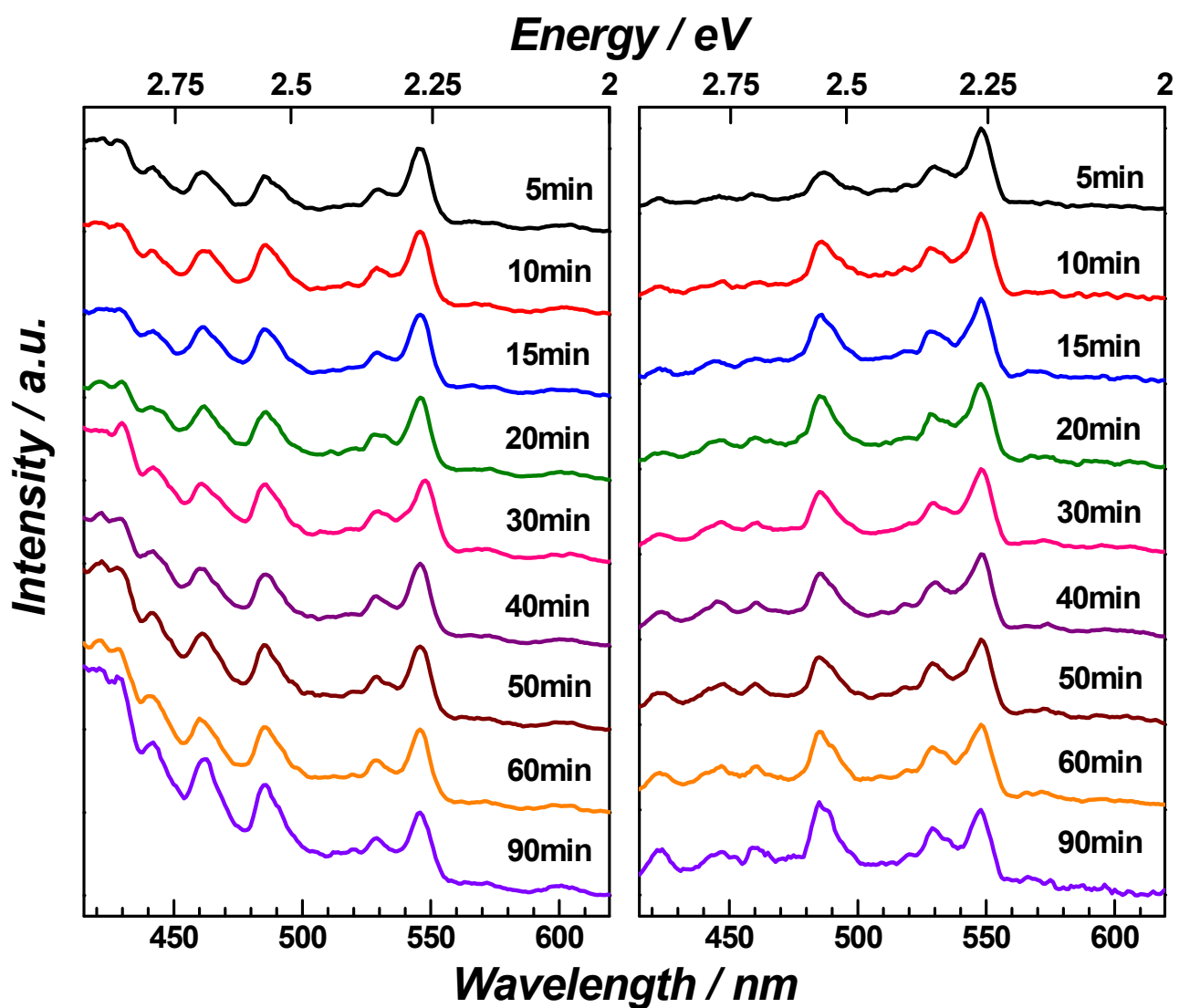


**Figure S3.** Photoluminescence spectra of  $\text{Cu}_2\text{O}$  nanoshells obtained at different reaction times during the Ostwald ripening process. The spectra shown in the left column and right column were excited at 402 nm and 190 nm, respectively.

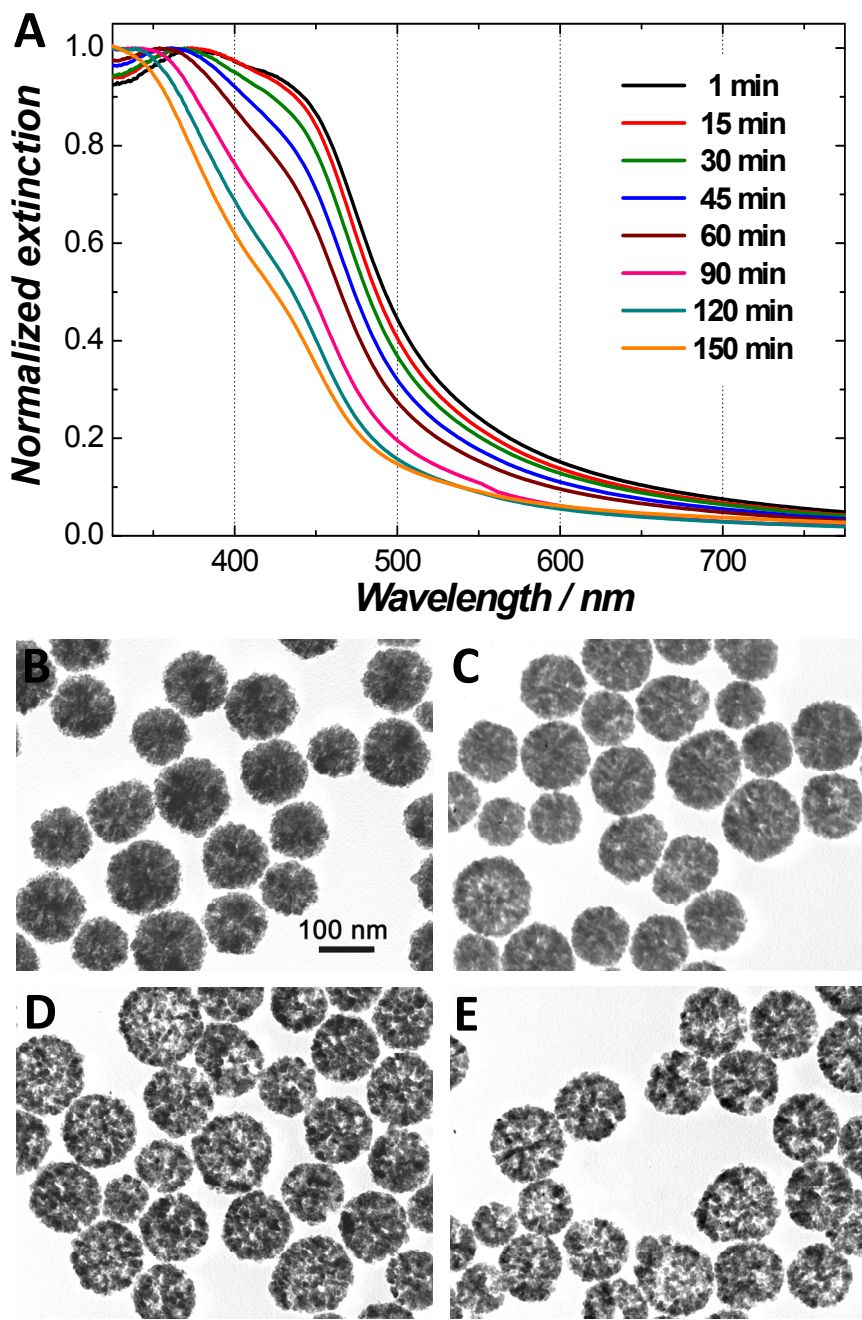


**Figure S4.** Symmetric hollowing of  $\text{Cu}_2\text{O}$  spherical particles with average outer radius of  $\sim 60$  nm in the presence of polyvinylpyrrolidone during Ostwald ripening. (A) Extinction spectra of the  $\text{Cu}_2\text{O}$  particles obtained at different reaction times. TEM images of  $\text{Cu}_2\text{O}$  particles obtained at different reaction times during Ostwald ripening: (B) 1 minute; (C) 30 minutes; (D) 60 minutes; and (E) 90 minutes. All the TEM images shown here share the same scale-bar in panel B.

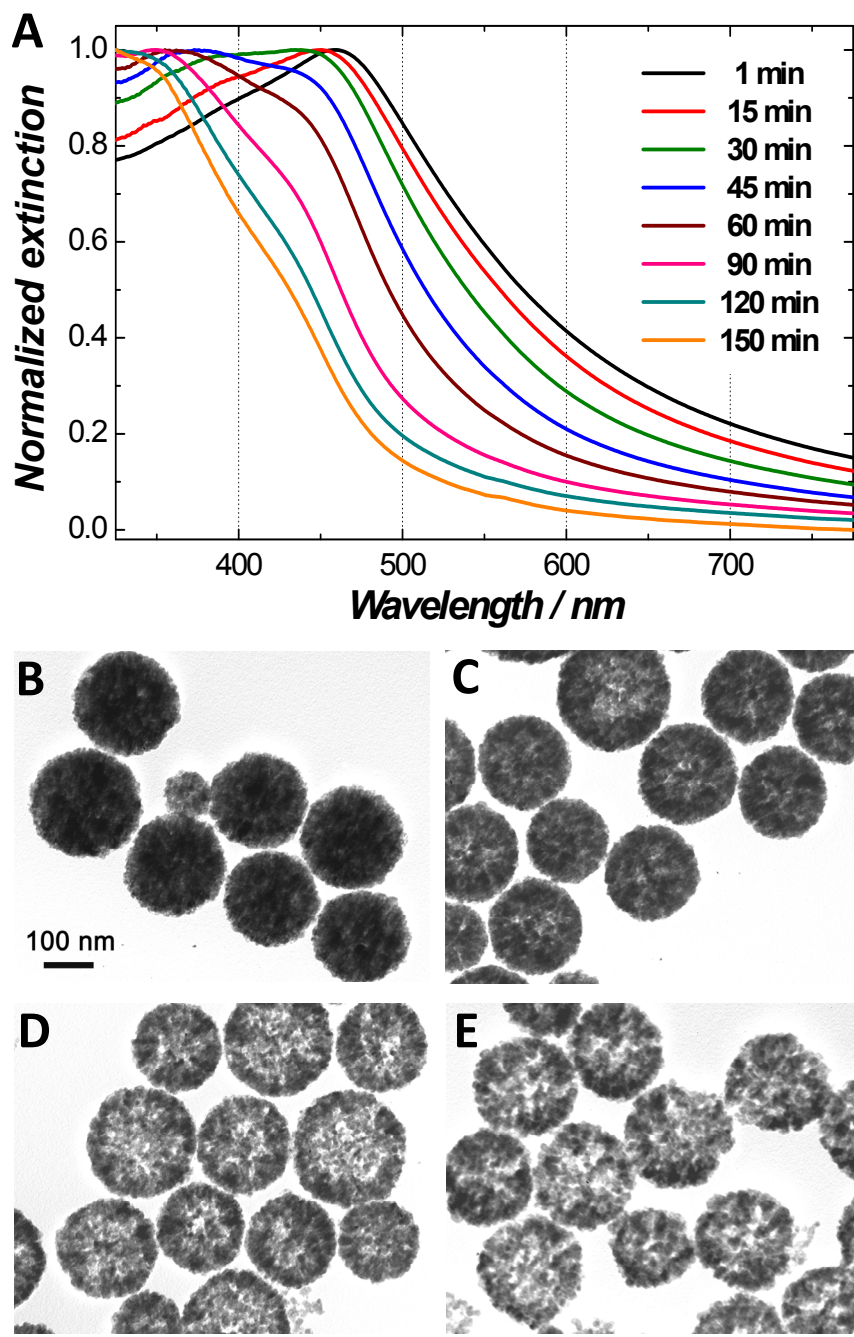


**Figure S5.** Symmetric hollowing of  $\text{Cu}_2\text{O}$  spherical particles with average outer radius of  $\sim 120$  nm in the presence of polyvinylpyrrolidone during Ostwald ripening. (A) Extinction spectra of the  $\text{Cu}_2\text{O}$  particles obtained at different reaction times. TEM images of  $\text{Cu}_2\text{O}$  particles obtained at different reaction times during Ostwald ripening: (B) 1 minute; (C) 30 minutes; (D) 60 minutes; and (E) 90 minutes. All the TEM images shown here share the same scale-bar in panel B.

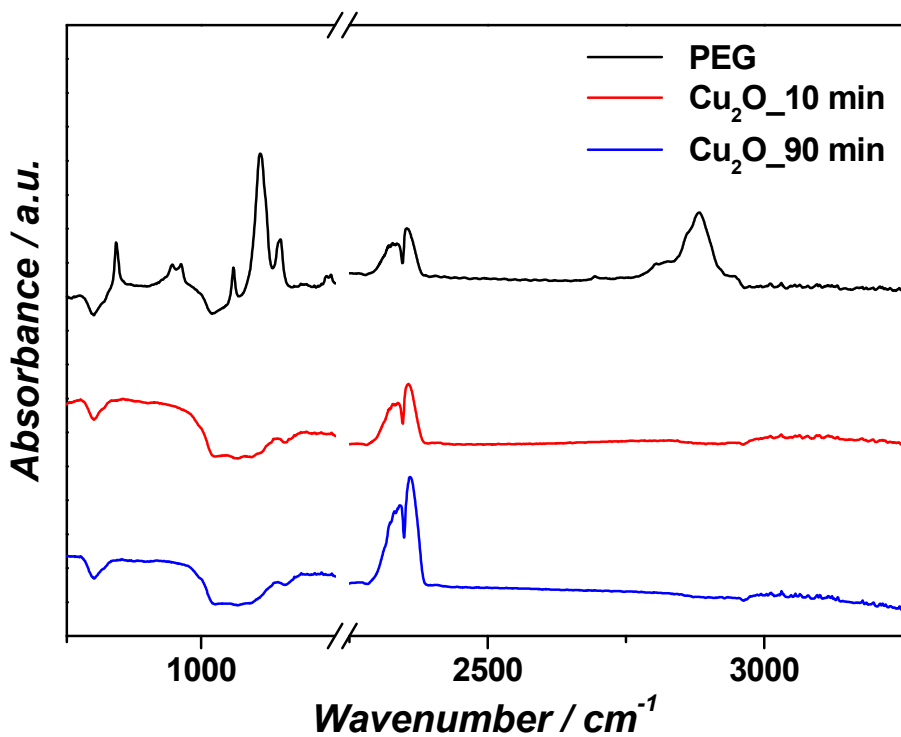


**Figure S6.** FT-IR spectra of pure PEG and Cu<sub>2</sub>O particles obtained at 10 minutes and 90 minutes during the PEG-mediated Ostwald ripening process. The double-peaked feature at 2360 cm<sup>-1</sup> and 2335 cm<sup>-1</sup> is corresponding to the CO<sub>2</sub> adsorbed on the surface of Cu<sub>2</sub>O particles.